Polarity-tunable anomalous Hall effect in magnetic topological insulator $MnBi_2Te_4$

Lixuan Tai[1], Su Kong Chong[1], Huairuo Zhang[2,3], Peng Zhang[1], Peng Deng[1], Christopher Eckberg[1,4-6], Gang Qiu[1], Bingqian Dai[1], Haoran He[1], Di Wu[1], Shijie Xu[1,7], Albert V. Davydov[3], and Kang L. Wang[1*]

1. Department of Electrical and Computer Engineering, University of California, Los Angeles, California 90095, United States

2. Theiss Research, Inc., La Jolla, California 92037, United States

3. Materials Science and Engineering Division, National Institute of Standards and Technology (NIST), Gaithersburg, Maryland 20899, United States

4. Fibertek Inc., Herndon, VA 20171

5. US Army Research Laboratory, Adelphi, MD 20783

6. US Army Research Laboratory, Playa Vista, CA 90094

7. Shanghai Key Laboratory of Special Artificial Microstructure and Pohl Institute of Solid State Physics and School of Physics Science and Engineering, Tongji University, Shanghai 200092, China

*Correspondence to: wang@ee.ucla.edu.

Abstract

The polarity-tunable anomalous Hall effect (AHE) is useful for electronic device applications. Here in a magnetic topological insulator $MnBi_2Te_4$ grown by molecular

beam epitaxy, we report the polarity change of the AHE by increasing the temperature or tuning the gate bias. This is possible because the anomalous Hall response is composed of two competing contributions with opposite polarities. The negative contribution is intrinsic to $MnBi_2Te_4$, follows an ambipolar gate response and has a larger coercivity with increasing thickness. Meanwhile, the positive one has a coercivity that is about one order of magnitude greater than the negative one, dominates the Hall response at higher temperatures, is more tunable by a gate bias and vanishes by increasing the thickness of the thin film. One possible explanation for the additional positive AHE is an extra surface ferromagnetism caused by the surface-state-mediated RKKY interaction among magnetic impurities on the surface. Our work provides the understanding of the AHE of $MnBi_2Te_4$, and paves the way for many device applications, e.g. energy-efficient voltage-controlled memory.

Since its discovery in 1881, the anomalous Hall effect (AHE) has found its use in numerous applications, including magnetic memories, magnetic sensors, magnetometry, etc.[1] Specifically, magnetic memories use the magnetic order in the material to store information, and have the advantages of non-volatility, low power consumption, and good shock resistance. As a reliable electrical indicator of magnetic order in materials, the AHE is commonly used in spintronic studies to read out the state of a magnetic memory. In such applications, current driven spin-torques may be used to write the magnetic state of a bit, with information being subsequently read out by the polarity of the anomalous Hall signal. [2,3] Switching magnetic bits using spin-torques is relatively inefficient, however, and often requires a large current to manipulate the sign of the AHE. The Joule heating associated with this writing current represents one of the dominant factors limiting the viability of such devices. It is therefore highly desirable to discover schemes where the polarity of the AHE may be tuned without applying a current, preferably by voltage only, as this reduces power consumption and relieves the Joule heating problem. The gate voltage tuning of the AHE polarity can also be made non-volatile by combining it with a ferroelectric material and serve as a direct Hall voltage indicator of the ferroelectric order. This all-voltage approach, once realized, might consume less power than conventional ferroelectric memories, which also require a large drain current to represent information.[4,5]

Among the various materials that exhibit the AHE, magnetic topological insulators (MTI) are notable as they can realize the quantized version of the AHE, the quantum anomalous Hall effect (QAHE)[6–10] and can host exotic quasiparticle excitations that behave as axions [11,12] and Majorana fermions[13,14], the latter of which has been shown to have potential for quantum computing. In addition, MTIs have very promising applications in energy-efficient magnetic memory devices, because their unique topological surface state enables efficient charge to spin conversion and magnetization manipulation.[15,16] Recently, $MnBi_2Te_4$ has been discovered as an intrinsic MTI. It has a layered tetradymite magnetic compound consisting of Te-Bi-Te-Mn-Te-Bi-Te septuple layers (SL) separated by van der Waals gaps (Fig. 1b). $MnBi_2Te_4$ is an A-type antiferromagnet (AFM), and it has a Néel temperature of 25.4 K. Each Mn^{2+} ion has an out-of-plane magnetic moment of about $5\mu_B$, which align parallel to each other within each SL, and anti-parallel between two neighboring SLs. Thin films of $MnBi_2Te_4$ can be made either through mechanical exfoliation of bulk crystals or molecular beam epitaxy (MBE), and intrinsically show a negative AHE (or QAHE) due to uncompensated magnetic moments. [9,10,17–26]

Apart from the AHE, another interesting type of Hall response is the topological Hall effect (THE), which usually emerges as "humps" in the Hall resistance when scanning magnetic field. This originates from the additional Berry phase acquired by electrons going through chiral spin textures such as magnetic skyrmions.[27–31] However, other reasons, such as symmetry-protected nodal lines, or the addition of two AHEs, could give rise to an AHE loop with humps that are similar to the THE.[32–34] These cases differentiate from the true THE by the fact that the anomalous Hall loop could be tuned to an opposite polarity. In the transport studies of structures containing topological insulators, including $(Bi,Sb)_2Te_3$/MnTe/CrSe heterostructures[31,32] , or V-doped $(Bi,Sb)_2Te_3$/$(Bi,Sb)_2Te_3$ heterostructures[33], the two AHEs are found to originate from two co-existing magnetic orders from the bulk and the surface. In fact, apart from transport, other experimental techniques, including X-ray absorption spectroscopy (XAS) , X-ray magnetic circular dichroism (XMCD) and angle-resolved photoemission spectroscopy (ARPES), have also clearly revealed the co-existence of the bulk and surface magnetisms in MTI (including Cr-doped Bi_2Se_3 and $MnBi_2Te_4$), and the surface magnetism can be even more robust than the bulk.[35–37]

In this Article, we demonstrate that in magnetic topological insulator $MnBi_2Te_4$ grown by molecular beam epitaxy, although the AHE loops bear humps that resemble the topological Hall effect from magnetic skyrmions, the polarity of the AHE can be tuned from negative to positive by increasing the temperature or tuning the gate bias from positive to negative. This can be explained by the superposition of two AHE loops with opposite polarities. The negative AHE is intrinsic to $MnBi_2Te_4$, follows an ambipolar gate response, and has enhanced coercivity with increasing thickness of the thin film. The positive AHE has a coercivity that is almost one order of magnitude greater than the negative AHE, decays much slower with increasing temperature, is more easily tuned by the top gate and vanishes with increasing thickness. One possible origin of the extra positive AHE is an additional surface ferromagnetism mediated by the surface-state-induced RKKY interaction among magnetic impurities on the surface. Our work provides the understanding of the AHE of $MnBi_2Te_4$ and has great potential for a number of electronic device applications. For example, the direct gate tuning of the AHE polarity without applying a current can be used for energy-efficient voltage-controlled memories.

Tuning the polarity of the AHE

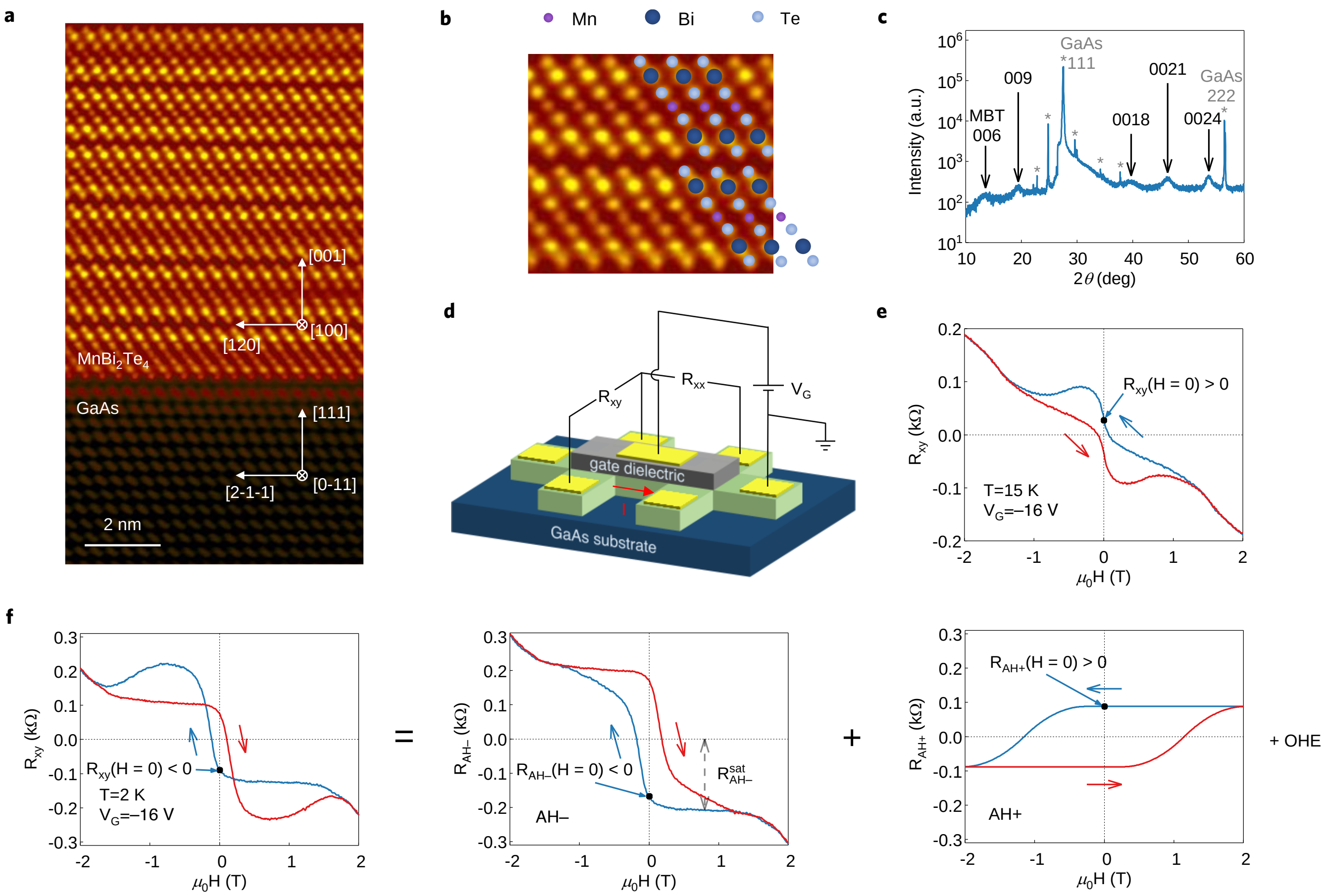

Figure 1. Material characterizations and the polarity change of the AHE. (a) A cross-sectional HAADF-STEM image showing the epitaxial growth of $MnBi_2Te_4$ film on the GaAs substrate. The image was taken along the [100] zone-axis of the $MnBi_2Te_4$ crystal. (b) A local zoom-in view of (a) overlaid with an atomic model of $MnBi_2Te_4$. (c) The XRD pattern of the 7 SL sample. Absence of all but 00*l* (*l*=6,9,18,21,24) reflections corroborates STEM's data about the single-crystalline nature of $MnBi_2Te_4$ film. The calculated c-lattice parameter is 40.876(3) Å. Note: the peaks from the substrate are marked with *. (d) A schematic of the Hall bar device structure with a top gate. (e) The Hall resistance of the 7 SL sample as a function of an applied out-of-plane magnetic field, showing an AHE loop with a positive polarity at T=15 K. The blue and red arrows indicate the direction of the field scan. (f) The AHE loop from the same device as (e)

with a negative polarity at T=2 K and its decomposition into the sum of two AHE loops, a negative AH– and a positive AH+. The saturated and zero-field Hall resistance of AH–, R_{AH-}^{sat} and $R_{AH-}(H = 0)$, and the zero-field Hall resistance of the AH+, $R_{AH+}(H = 0)$ are labeled as defined.

In this work, the thin films were grown on GaAs (111)B substrates by molecular beam epitaxy, and various characterization methods are used to characterize the microstructural properties of the thin film. During growth, *in-situ* reflection high-energy electron diffraction (RHEED) showed sharp 1 × 1 diffraction streaks, indicating good epitaxial crystal quality and flat surface morphology (see Fig. S1 in the supplementary information). High-angle annular dark field scanning transmission electron microscopy (HAADF-STEM) was further carried out to study the atomic structures of the thin film. Figure 1a and b show the HAADF-STEM images with atomic resolution from a cross-sectional specimen. The images clearly show the characteristic septuple layer (SL) substructures of rhombic $MnBi_2Te_4$ epitaxially grown on cubic GaAs (111)B substrate with crystallographic relationships of $(001)_R \parallel (111)_C$ and $[100]_R \parallel [0\text{-}11]_C$. Heavier elements also reveal sharper contrasts (Bi>Te>Mn), which is consistent with the sequence of Te-Bi-Te-Mn-Te-Bi-Te in the SL structures. [21] X-ray diffraction (XRD) was also performed to characterize the film's crystal structure. The XRD pattern in Fig. 1c shows five 00*l* (*l*=6,9,18,21,24) reflections from the $MnBi_2Te_4$ film and two high-intensity 111 and 222 peaks from GaAs, thus confirming the $(001)_R \parallel (111)_C$ epitaxial growth. The out-of-plane lattice constant c=40.876 ± 0.003 Å is calculated from the 00*l* XRD reflections (which comprises of 3 SLs, so that 1 SL= 13.63 Å), while the in-plane lattice constant a=4.32 ± 0.02 Å is extracted from the RHEED streaks. Both of the values align well with previous reports of the $MnBi_2Te_4$ lattice parameter values. [19,25] All the sharp, narrow peaks in the XRD pattern can be identified from the GaAs substrate and marked with * (see Fig. S2 in the supplementary information). Cross-sectional HAADF-STEM images of the thin film also reveal additional local structures, including Bi_2Te_3 quintuple layers, $BiTe_2$ monolayers caused by Mn line vacancies in the $MnBi_2Te_4$ septuple layers, and a $MnTe_2$ monolayer on the surface of the thin film that interfaces with Bi_2Te_3. (see Fig. S3 in the supplementary information) We will discuss the possible effects of these additional local structures in detail later.

Samples with various thicknesses were grown with the same method, including 4 SL, 5 SL, 6 SL, 7 SL, 9 SL, 12 SL, 18 SL, 24 SL, 48 SL. Since the film is dominantly in the $MnBi_2Te_4$ phase, the thickness of the thin films is counted in SLs, where 1 SL= 13.63 Å. Two types of Hall bar devices were fabricated to characterize the transport properties: one type is millimeter-sized, has no gate and an aspect ratio of 2:1 and was made for all the samples; another type is micron-sized, has a top gate and an aspect ratio of 1:1 (as in Fig. 1d), and was made for the 7 SL sample only. The longitudinal (R_{xx}) and Hall resistance (R_{xy}) were obtained while sweeping an out-of-plane external magnetic field H.

Two different types of anomalous Hall loops emerge from the same device: one has a positive polarity as in Fig. 1e and one has a negative polarity as in Fig. 1f as well as humps that resemble the topological Hall effect from magnetic skyrmions. Here we define the polarity of the AHE as the sign of $R_{xy}(H = 0)$, i.e. the Hall resistance at zero external magnetic field after scanning from +2 T to the zero field. The change of the

AHE polarity can be explained by the superposition of two anomalous Hall loops, a negative AH– and a positive AH+, which is expressed in the following equation

$$R_{xy} = R_{AH-} + R_{AH+} + \alpha_{OHE}H$$

where R_{AH-} and R_{AH+} are the Hall resistance of AH– and AH+ and the constant α_{OHE} is the slope of the linear ordinary Hall effect (OHE). The fitted results of AH– and AH+ are presented in Fig. 1f. The saturated and zero-field Hall resistance of AH–, R_{AH-}^{sat} and $R_{AH-}(H = 0)$, along with the zero-field Hall resistance of the AH+, $R_{AH+}(H = 0)$, are labeled in Fig. 1f as defined. Notably, the coercivity of the AH+ (H_{C+}) is 1.15 T, which is almost one order of magnitude larger than the coercivity of the AH– (H_{C-}), 0.18 T.

Temperature and gate dependence

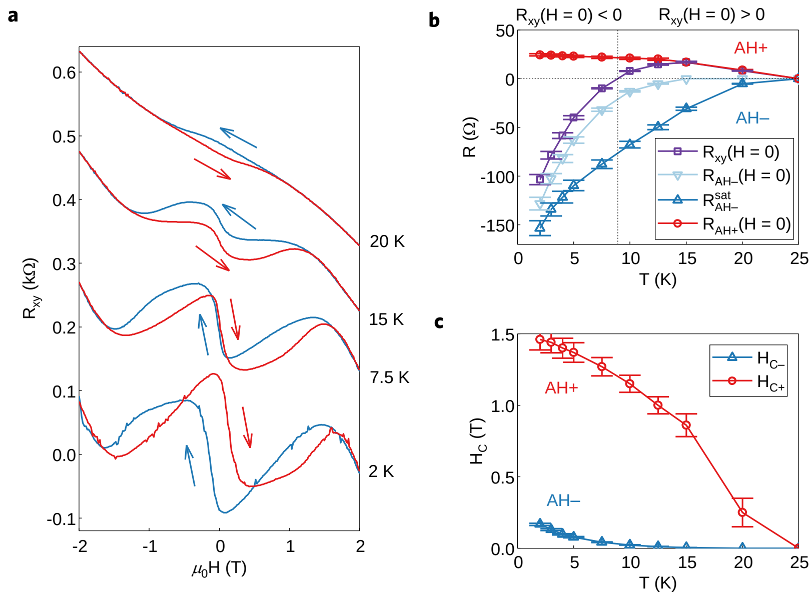

Figure 2. The temperature dependence of the AHE in the 5 SL sample (the Hall bar device with no gate). (a) The Hall resistance R_{xy} as a function of out-of-plane magnetic field H under various temperatures, with blue and red arrows indicating the direction of the field scan. (b) The temperature dependence of the saturated and zero-field Hall resistance of AH–, R^{sat}_{AH-} and $R_{AH-}(H = 0)$ (defined in Fig. 1) and the zero-field Hall resistance of the AH+, $R_{AH+}(H = 0)$. (c) The coercivities of AH– and AH+, H_{C-} and H_{C+} as a function of temperature.

As presented in Fig. 2, the temperature dependence reveals a polarity change of the AHE and shows that AH– and AH+ have close critical temperatures, but AH+ keeps having a significantly larger coercivity than AH– and decays much slower with increasing temperature. As temperature increases, the AHE loops evolve from a negative one with humps to a single positive one, indicating that the positive AH+ becomes dominant. The signs of $R_{xy}(H = 0)$ also indicate the polarity change of the AHE from negative to positive. The AHE vanishes above 25 K, which is consistent with previous reports of the Néel temperature of $MnBi_2Te_4$.[17,18,26] The two anomalous Hall components, AH– and AH+ are fitted from the AHE loops (see Fig. S4 in the supplementary information), and key parameters are extracted and plotted against temperature. With the increase of temperature, R_{AH-}^{sat} decreases quickly and vanishes above 25 K, and $R_{AH-}(H = 0)$ decreases even more quickly and becomes zero beyond 15 K. In comparison, $R_{AH+}(H = 0)$ follows a much slower trend of decrease with increasing temperature, changes very little below 15 K and also vanishes above 25 K. The coercivities also follow a similar trend, as H_{C-} also decreases much faster than H_{C+} with increasing temperature, and always stay at least one order of magnitude smaller than H_{C+}. The analysis above shows that both AH– and AH+ have the close critical temperatures of 25 K, but AH+ is more robust than AH– in terms of temperature evolution and coercive field.

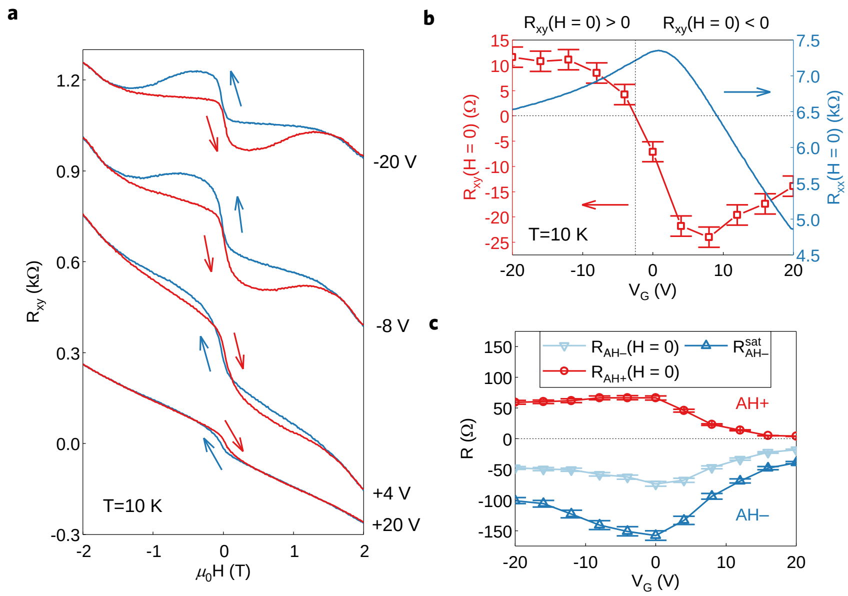

Figure 3. The gate dependence of the AHE in the 7 SL sample (the Hall bar device with a top gate). (a) The Hall resistance R_{xy} as a function of out-of-plane magnetic field H under various gate biases at T=10 K, with blue and red arrows indicating the direction of the field scan. (b) The gate dependence of the zero-field Hall and longitudinal resistance, $R_{xy}(H=0)$ and $R_{xx}(H=0)$ at T=10 K. (c) The gate dependence of the saturated and zero-field Hall resistance of AH–, R_{AH-}^{sat} and $R_{AH-}(H=0)$, and the zero-field Hall resistance of AH+, $R_{AH+}(H=0)$. (defined in Fig. 1)

The gate dependence shown in Fig. 3 also reveals a polarity change of the AHE, which can be useful for applications such as energy-efficient voltage-controlled memories. Moreover, it demonstrates that AH+ is more tunable by the top gate than AH–. As the gate voltage sweeps from -20 V to +20 V, the AHE loops evolve from a positive one with humps to a single negative one. The sign of $R_{xy}(H=0)$ also shows the polarity change of the AHE from positive to negative. Meanwhile, $R_{xx}(H=0)$ follows an ambipolar response to the gate voltage. Similarly, the two anomalous Hall components, AH– and AH+ are fitted from the AHE loops as well (see Fig. S5 in the supplementary information) to examine their gate dependence. Both R_{AH-}^{sat} and $R_{AH-}(H=0)$ follow an ambipolar response to the gate voltage. Interestingly, the amplitude of AH+, $R_{AH+}(H=0)$ almost saturates at negative gate voltage and decreases rapidly at positive gate voltage, which is distinct from the previous ambipolar behavior. The AH+ is more tunable by the top gate than AH–, as indicated by the fact that the amplitude of AH+ changes by a factor of 16.7, while AH– changes by a factor of only 4.1.

Thickness dependence

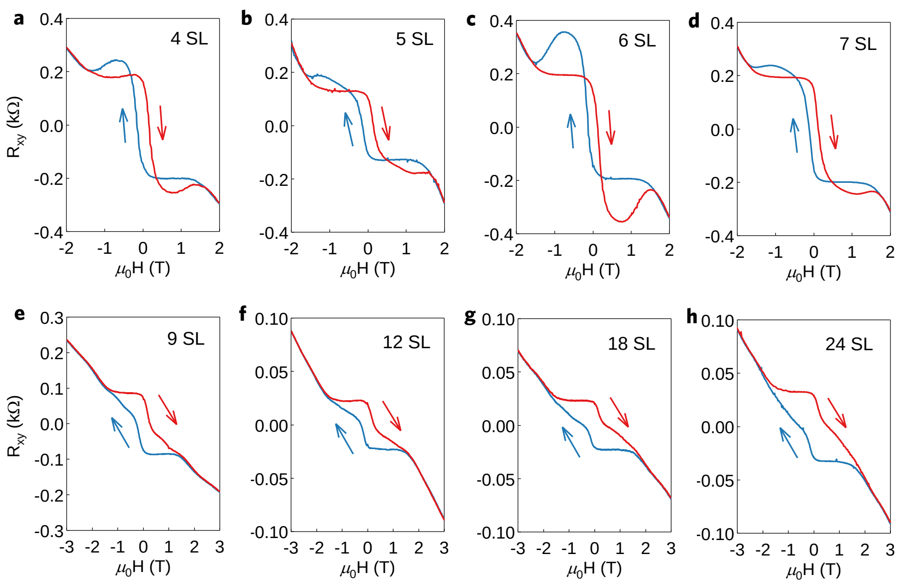

Figure 4. The thickness dependence of the AHE (Hall bar devices with no gate). (a)-(h) The Hall resistance of samples with various thicknesses as a function of out-of-plane magnetic field H at T=2 K, with blue and red arrows indicating the direction of the field scan. The linear ordinary Hall backgrounds are removed.

Thickness (SL)	4	5	6	7	9	12	18	24	48
Have humps	Yes	Yes	Yes	Yes	No	No	No	No	No
H_C (T)	0.16	0.15	0.13	0.12	0.27	0.25	0.44	0.55	0.51

Table 1. The existence of humps in the AHE loops and the coercivity (H_C) of the AHE for samples with various thicknesses.

The thickness dependence of the AHE loops, as presented in Fig. 4, reveals that the humps vanish with increasing thickness of the thin film (see Fig. S6 in the supplementary information for the data of the 48 SL sample). In order to extract the coercivity from the intersection of the AHE loops and the x-axis, the linear ordinary Hall backgrounds have been subtracted around the saturation field of ~0.7 T (when scanning from +2 T to -2 T). All the samples show a negative AHE under the temperature at T=2 K. However, the humps in the AHE only appears between 4 to 7 SL and vanishes for the thickness of 9 SL and beyond. As the hump vanishes and the thickness further increases, the coercivities also tend to increase to a large extent, although not monotonously, as are listed in Table 1.

Possible physical origin

The negative AH– is intrinsic to $MnBi_2Te_4$ [9,21], while the origin of the additional positive AH+ is still not clear. Here we speculate that the additional positive AH+ is due to an extra surface ferromagnetism from surface-state-mediated RKKY (Ruderman–Kittel–

Kasuya–Yosida) interactions among ferromagnetic impurities on the surface (a $MnTe_2$ monolayer). However, this phenomenon is still open to other explanations as well.

The reasons are outlined here, and a detailed version is presented in the Section 5 of the supplementary information. Since AH+ vanishes with increasing thickness, as shown in Fig. 4, AH+ might originate from an additional surface ferromagnetism. Because AH+ almost saturates at negative gate voltages and drops rapidly as the gate voltage sweeps from zero to positive, as presented in Fig. 3, we think AH+ might depend on hole carriers and thus originate from hole-mediated RKKY interactions, which agrees with previous results of surface ferromagnetism in MTI. [38–43] From the HAADF-STEM iamges, among the additional local structures in our thin films (see Fig. S3 in the supplementary information), the ferromagnetic $MnTe_2$ monolayer[44,45] on the surface is the most likely to contribute to the positive AH+. Because AH+ has a critical temperature of 25 K, which is the same as that of $MnBi_2Te_4$ and different from that of a $MnTe_2$ monolayer itself (88 K to 440 K)[44,45] as demonstrated in Fig. 2, the interfacial $MnTe_2$ monolayer may have a similar mechanism of surface ferromagnetism as the MTI $MnBi_2Te_4$[35–37,40]. On the surface, the Dirac electronic states of a topological insulator mediate an RKKY interaction among the magnetic impurities, contributing to the surface ferromagnetism. [46–48]

Conclusions

In conclusion, in the magnetic topological insulator $MnBi_2Te_4$ grown by molecular beam epitaxy, a AHE loop with humps was observed and its polarity was shown to change with temperature or gate bias. We attribute this to the superposition of two AHEs, one negative (AH–) and one positive (AH+). AH– is intrinsic to $MnBi_2Te_4$, follows an ambipolar gate response and has larger coercivity with increasing thickness. Meanwhile, AH+ has a much greater coercivity than AH–, decreases slower with increasing temperature, shrinks significantly with increasing positive gate bias, and vanishes in thicker films. It is speculated that AH+ originates from an extra surface ferromagnetism, which arises from the surface-state-mediated RKKY interaction among ferromagnetic impurities (a $MnTe_2$ monolayer) on the surface. This work provides the understanding of the AHE of $MnBi_2Te_4$ and may be potentially useful for electronic applications. For example, the change in the polarity of AHE with gate bias can be used for energy-efficient memories.

Methods

Growth of materials. All the materials in this paper were grown in an ultra-high vacuum, Perkin-Elmer molecular beam epitaxy (MBE) system. We used epi-ready semi-insulating GaAs (111)B substrates for the growth. The entire process was monitored by the reflection high-energy electron diffraction (RHEED) *in situ*, where the digital RHEED images were captured using a KSA400 system built by K-space Associates, Inc. Before growth, the substrates were loaded into the MBE chamber and pre-annealed at the temperature of 630 °C in a Te-rich environment to desorb the oxide on the surface. During growth, we kept the substrate at 200 °C. High-purity Mn, Bi and Te were evaporated simultaneously from standard Knudsen cells. After the deposition, the film was post-annealed in a Te-rich environment at 290 °C for 2 minutes to improve crystallinity. The sharp and streaky lines in the RHEED pattern indicate good epitaxial crystal quality.

Material characterizations. The X-ray diffraction (XRD) measurements were performed on the 7 SL sample using an X-ray powder diffractometer with Cu Kα radiation (Panalytical X'Pert Pro). The HAADF-STEM characterization was performed on the 24 SL sample with FEI Nova NanoLab 600 DualBeam (SEM/FIB). Initially, 0.5 μm thick Pt was deposited by electron beam-induced deposition on top of the thin film sample to protect its surface. After that, 1 μm Pt was deposited by ion beam-induced deposition. In the final step of preparation, the sample was cleaned with 2 kV Ga-ions using a low beam current of 29 pA and a small incident angle of 3 degrees to reduce Ga-ions damage. An FEI Titan 80-300 probe-corrected STEM/TEM microscope operating at 300 keV was employed to acquire atomic-resolution HAADF-STEM images.

Transport measurements. For the micron-sized Hall bar device with a top gate, the thin film was fabricated into a 40 μm (length) × 40 μm (width) Hall bar geometry using a standard photolithography process. Cr/Au contact electrodes with thicknesses of 10/100 nm were deposited using an electron beam evaporator. Mica and graphite thin flakes, which serve as the gate dielectric and the electrode, respectively, were exfoliated and subsequently transferred onto the as-fabricated Hall bar device for top gating. For the millimeter-sized Hall bar devices without a gate, the thin films were fabricated into Hall bar patterns with the dimensions of 10 mm (length) × 5 mm (width) using standard etching with a hard mask. Indium contacts were later soldered onto the devices. Low temperature magnetoelectric transport measurements were conducted in a Quantum Design physical property measurement system (PPMS) equipped with a 9 T superconducting magnet with a base temperature of 1.9 K. A Keithley 6221 current source was used to generate a source AC current of 0.1 μA at 8.3 Hz (for the micron-sized Hall bar device with a top gate) or 1 μA at 15.38 Hz (for the millimeter-sized Hall bar devices without a gate), and multiple lock-in amplifiers (Stanford Research SR830) were used to obtain longitudinal and Hall resistance from the Hall bar devices. Gate voltage was applied to the gate electrode of the micron-sized Hall bar device and swept by a Keithley 2636 source meter.

References

1. Takahashi, H. Magnetic field sensor utilizing anomalous hall effect magnetic film. (2001).

2. Bhatti, S. *et al.* Spintronics based random access memory: a review. *Mater. Today* **20**, 530–548 (2017).

3. Shao, Q. *et al.* Room Temperature Highly Efficient Topological Insulator/Mo/CoFeB Spin-Orbit Torque Memory with Perpendicular Magnetic Anisotropy. *Tech. Dig. - Int. Electron Devices Meet. IEDM* **2018-Decem**, 36.3.1-36.3.4 (2019).

4. Das, S. & Appenzeller, J. FETRAM. An organic ferroelectric material based novel random access memory cell. *Nano Lett.* **11**, 4003–4007 (2011).

5. Park, J. H., Nayak, P. K. & Alshareef, H. N. Novel Ferroelectric Polymer Memory Coupling Two Identical Thin-Film Transistors. *Adv. Electron. Mater.* **2**, 2–7 (2016).

6. Chang, C. Z. *et al.* Experimental observation of the quantum anomalous Hall effect in a magnetic topological Insulator. *Science* **340**, 167–170 (2013).

7. Kou, X. *et al.* Metal-to-insulator switching in quantum anomalous Hall states. *Nat. Commun.* **6**, 1–8 (2015).

8. Kou, X. *et al.* Scale-invariant quantum anomalous hall effect in magnetic topological insulators beyond the two-dimensional limit. *Phys. Rev. Lett.* **113**, 1–5 (2014).

9. Deng, Y. *et al.* Quantum anomalous Hall effect in intrinsic magnetic topological insulator MnBi2Te4. *Science* **367**, 895–900 (2020).

10. Deng, H. *et al.* Observation of high-temperature quantum anomalous Hall regime in intrinsic MnBi2Te4/Bi2Te3 superlattice. *Nat. Phys.* doi:10.1038/s41567-020-0998-2 (2020).

11. Xiao, D. *et al.* Realization of the Axion Insulator State in Quantum Anomalous Hall Sandwich Heterostructures. *Phys. Rev. Lett.* **120**, 56801 (2018).

12. Liu, C. *et al.* Robust axion insulator and Chern insulator phases in a two-dimensional antiferromagnetic topological insulator. *Nat. Mater.* **19**, (2020).

13. He, Q. L. *et al.* Chiral Majorana fermion modes in a quantum anomalous Hall insulator–superconductor structure. *Science* **357**, 294–299 (2017).

14. Peng, Y. & Xu, Y. Proximity-induced Majorana hinge modes in antiferromagnetic topological insulators. *Phys. Rev. B* **99**, 1–9 (2019).

15. Che, X. *et al.* Strongly Surface State Carrier-Dependent Spin–Orbit Torque in Magnetic Topological Insulators. *Adv. Mater.* **1907661**, 1–9 (2020).

16. Fan, Y. *et al.* Magnetization switching through giant spin-orbit torque in a magnetically doped topological insulator heterostructure. *Nat. Mater.* **13**, 699–704 (2014).

17. Zeugner, A. *et al.* Chemical Aspects of the Candidate Antiferromagnetic Topological Insulator MnBi 2 Te 4. *Chem. Mater.* **31**, 2795–2806 (2019).

18. Ding, L. *et al.* Crystal and magnetic structures of magnetic topological insulators MnBi2Te4 and MnBi4Te7. *Phys. Rev. B* **101**, 1–6 (2020).

19. Lee, D. S. *et al.* Crystal structure, properties and nanostructuring of a new layered chalcogenide semiconductor, Bi2MnTe4. *CrystEngComm* **15**, 5532–5538 (2013).

20. Otrokov, M. M. *et al.* Prediction and observation of an antiferromagnetic topological insulator. *Nature* **576**, 416–422 (2019).

21. Gong, Y. *et al.* Experimental Realization of an Intrinsic Magnetic Topological Insulator. *Chinese Phys. Lett.* **36**, (2019).

22. Hirahara, T. *et al.* Large-Gap Magnetic Topological Heterostructure Formed by Subsurface Incorporation of a Ferromagnetic Layer. *Nano Lett.* **17**, 3493–3500 (2017).

23. Rienks, E. D. L. *et al.* Large magnetic gap at the Dirac point in Bi2Te3/MnBi2Te4 heterostructures. *Nature* (2019). doi:10.1038/s41586-019-1826-7

24. Ge, J. *et al.* High-Chern-Number and High-Temperature Quantum Hall Effect without Landau Levels. *Natl. Sci. Rev.* **7**, 1280–1287 (2020).

25. Yan, J. Q. *et al.* Crystal growth and magnetic structure of MnBi2Te4. *Phys. Rev. Mater.* **3**, 1–8 (2019).

26. Li, H. *et al.* Antiferromagnetic topological insulator MnBi2Te4: Synthesis and magnetic properties. *Phys. Chem. Chem. Phys.* **22**, 556–563 (2020).

27. Wu, Y. *et al.* N\’eel-type skyrmion in WTe2/Fe3GeTe2 van der Waals heterostructure. *Nat. Commun.* **11**, 3860 (2020).

28. Shao, Q. *et al.* Topological Hall effect at above room temperature in heterostructures composed of a magnetic insulator and a heavy metal. *Nat. Electron.* **2**, 182–186 (2019).

29. Lee, A. J. *et al.* Probing the Source of the Interfacial Dzyaloshinskii-Moriya Interaction Responsible for the Topological Hall Effect in Metal/Tm3Fe5O12 Systems. *Phys. Rev. Lett.* **124**, 1–5 (2020).

30. Liu, C. *et al.* Dimensional Crossover-Induced Topological Hall Effect in a Magnetic Topological Insulator. *Phys. Rev. Lett.* **119**, 1–5 (2017).

31. He, Q. L. *et al.* Exchange-biasing topological charges by antiferromagnetism. *Nat. Commun.* **9**, 1–8 (2018).

32. Chen, P. *et al.* Tailoring the hybrid anomalous hall response in engineered magnetic topological insulator heterostructures. *Nano Lett.* (2020). doi:10.1021/acs.nanolett.9b04932

33. Fijalkowski, K. M. *et al.* Coexistence of Surface and Bulk Ferromagnetism Mimics Skyrmion Hall Effect in a Topological Insulator. *Phys. Rev. X* **10**, 11012 (2020).

34. Sohn, B. *et al.* Sign-tunable anomalous Hall effect induced by symmetry-protected nodal structures in ferromagnetic perovskite oxide thin films. *arXiv Prepr.* arXiv:1912.04757 (2019).

35. Shikin, A. M. *et al.* Nature of the Dirac gap modulation and surface magnetic interaction in axion antiferromagnetic topological insulator MnBi$_2$Te$_4$. *Sci. Rep.* 1–13 (2020). doi:10.1038/s41598-020-70089-9

36. Nevola, D. *et al.* Coexistence of Surface Ferromagnetism and Gapless Topological State in MnBi$_2$Te$_4$. *Phys. Rev. X* **117205**, 1–5 (2020).

37. Liu, W. *et al.* Experimental observation of dual magnetic states in topological insulators. *Sci. Adv.* **5**, 4–10 (2019).

38. Kou, X. *et al.* Manipulating surface-related ferromagnetism in modulation-doped topological insulators. *Nano Lett.* **13**, 4587–4593 (2013).

39. Kou, X. *et al.* Interplay between different magnetisms in Cr-doped topological insulators. *ACS Nano* **7**, 9205–9212 (2013).

40. Checkelsky, J. G., Ye, J., Onose, Y., Iwasa, Y. & Tokura, Y. Dirac-fermion-mediated ferromagnetism in a topological insulator. *Nat. Phys.* **8**, 729–733 (2012).

41. Chang, C. Z. *et al.* Thin films of magnetically doped topological insulator with carrier-independent long-range ferromagnetic order. *Adv. Mater.* **25**, 1065–1070 (2013).

42. Li, M. *et al.* Experimental verification of the van Vleck nature of long-range ferromagnetic order in the vanadium-doped three-dimensional topological insulator Sb2Te3. *Phys. Rev. Lett.* **114**, 1–5 (2015).

43. Sessi, P. *et al.* Dual nature of magnetic dopants and competing trends in topological insulators. *Nat. Commun.* **7**, 1–6 (2016).

44. Chen, W., Zhang, J. min, Nie, Y. Z., Xia, Q. L. & Guo, G. H. Electronic structure and magnetism of MTe2 (M = Ti, V, Cr, Mn, Fe, Co and Ni) monolayers. *J. Magn. Magn. Mater.* **508**, (2020).

45. Chen, W., Zhang, J. M., Nie, Y. Z., Xia, Q. L. & Guo, G. H. Tuning magnetic properties of single-layer MnTe2 via strain engineering. *J. Phys. Chem. Solids* **143**, 109489 (2020).

46. Liu, Q., Liu, C. X., Xu, C., Qi, X. L. & Zhang, S. C. Magnetic impurities on the surface of a topological insulator. *Phys. Rev. Lett.* **102**, 1–4 (2009).

47. Biswas, R. R. & Balatsky, A. V. Impurity-induced states on the surface of three-dimensional topological insulators. *Phys. Rev. B* **81**, 1–4 (2010).

48. Rosenberg, G. & Franz, M. Surface magnetic ordering in topological insulators with bulk magnetic dopants. *Phys. Rev. B* **85**, 1–7 (2012).

Acknowledgments

The authors acknowledge the support from the National Science Foundation (NSF) (DMR-1411085 and DMR-1810163) and the Army Research Office Multidisciplinary University Research Initiative (MURI) under grant numbers W911NF16-1-0472 and W911NF-19-S-0008. In addition, H.Z. acknowledges support from the U.S. Department of Commerce, NIST under financial assistance award 70NANB19H138. A.V.D. acknowledges support from the Material Genome Initiative funding allocated to NIST. C.E. is an employee of Fibertek, Inc. and performs in support of Contract No. W15P7T19D0038, Delivery Order W911-QX-20-F-0023. The views expressed are those of the authors and do not reflect the official policy or position of the Department of Defense or the US government. The identification of any commercial product or tradename does not imply endorsement or recommendation by Fibertek Inc.

Author contributions

L.T. and K.L.W. conceived and designed the experiments. K.L.W. supervised the work. L.T. grew the samples, performed the X-ray diffraction and fabricated the millimeter-sized Hall bar devices. S.K.C. fabricated the micron-sized Hall bar device and transferred the top gate. L.T. and S.K.C. carried out the transport experiments. H.Z. and A.V.D. performed the transmission electron microscopy measurement. L.T. processed the data. All authors contributed to the analyses. L.T. and K.L.W. wrote the manuscript with contributions from all authors.

Competing interests

The authors declare no competing interests.

Supplementary Information

1. The RHEED patterns

The reflection high-energy electron diffraction (RHEED) patterns were captured *in situ* during the molecular beam epitaxy growth.

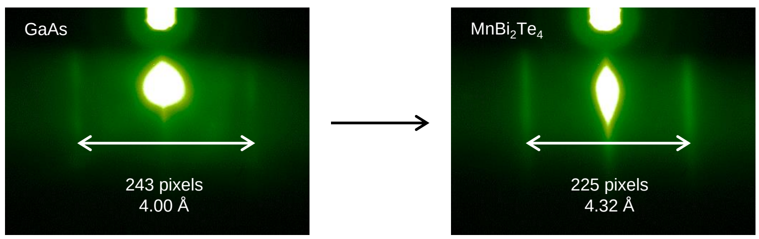

Figure S1. The RHEED patterns before and after the growth.

The sharp 1 × 1 diffraction streaks in the RHEED pattern indicate good epitaxial crystal quality and flat surface morphology. Because the spacing between the two first order diffraction streaks (*d*-spacing) is inversely proportional to the in-plane lattice constant, the in-plane lattice constant a=4.32 ± 0.02 Å is extracted from the RHEED streaks.

2. The XRD patterns

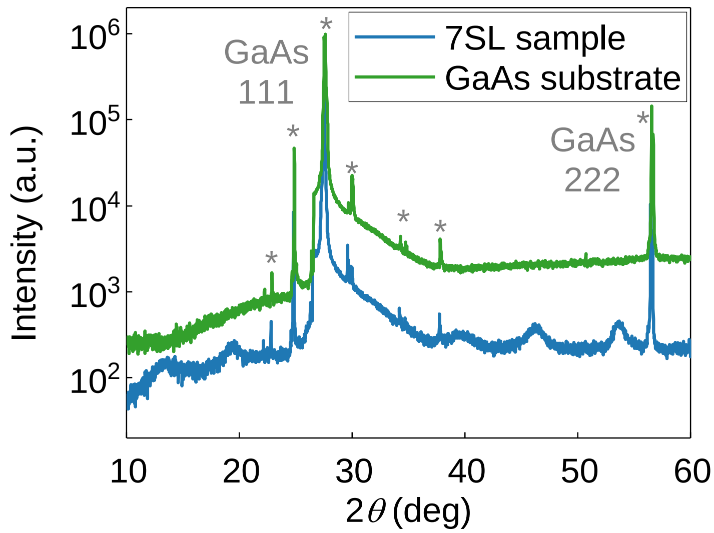

Figure S2. The XRD patterns of the 7 SL sample and the bare GaAs substrate. The peaks from the substrate are marked with *.

All the sharp, narrow peaks in the XRD patterns can be identified from the GaAs substrate. Apart from the 111 and 222 peaks from GaAs, the substrate also gives extra peaks, which might come from Cu Kβ radiation or the radiation from other Cu-cathode contaminations.

3. Additional local structures

Cross-sectional HAADF-STEM images of the thin film also reveal additional local structures, including Bi_2Te_3 quintuple layers, $BiTe_2$ monolayers caused by Mn line vacancies in the $MnBi_2Te_4$ septuple layers, and a $MnTe_2$ monolayer on the surface of the thin film that interfaces with Bi_2Te_3.

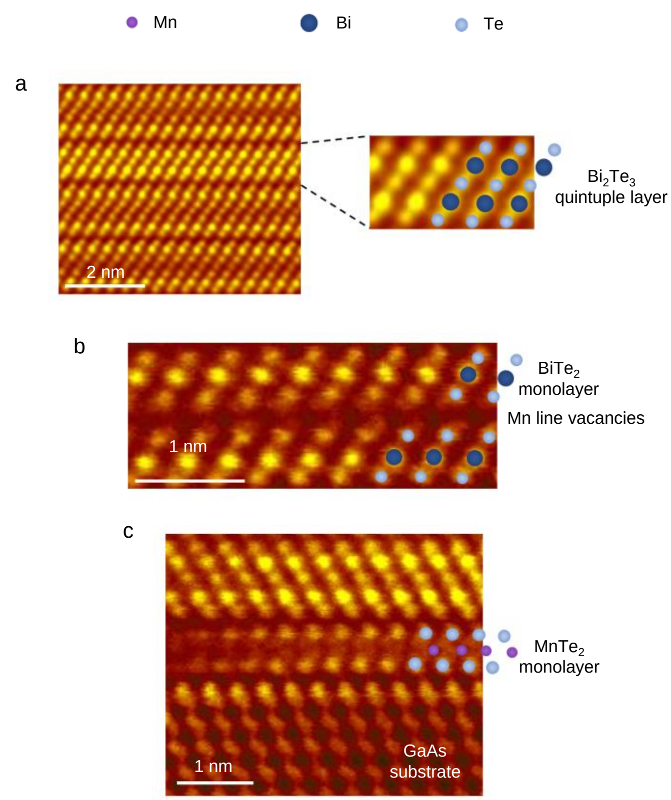

Figure S3. Additional cross-sectional HAADF-STEM images of the thin film, showing (a) a Bi_2Te_3 quintuple layer, (b) two $BiTe_2$ monolayers caused by Mn line vacancies in the $MnBi_2Te_4$ septuple layers and (c) a $MnTe_2$ monolayer on the surface of the thin film that interfaces with Bi_2Te_3.

4. Hall resistance data and their decompositions

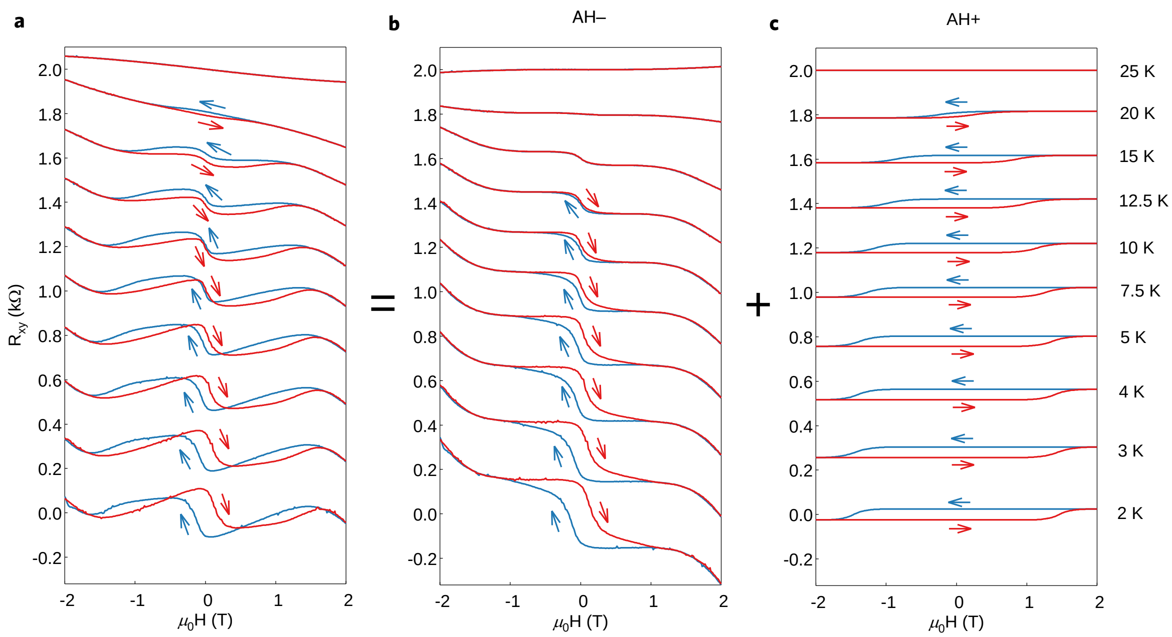

Figure S4. The temperature dependence of the AHE in the 5 SL sample (the Hall bar device with no gate). (a) shows the original data under various temperatures, with blue and red arrows indicating the direction of the field scan. (b) and (c) present the two AHEs that are obtained by decomposing the original data (AH– and AH+).

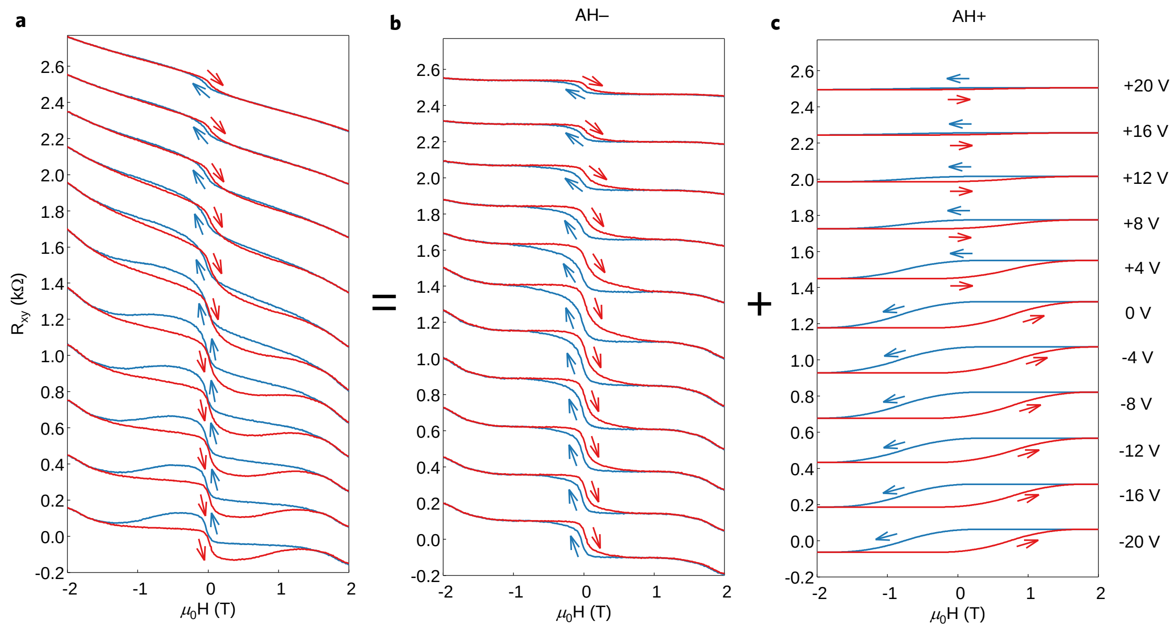

Figure S5. The gate dependence of the AHE in the 7 SL sample (the Hall bar device with a top gate) at T=10 K. (a) shows the original data under various gate biases, with blue and red arrows indicating the direction of the field scan. (b) and (c) present the two AHEs that are obtained by decomposing the original data (AH– and AH+).

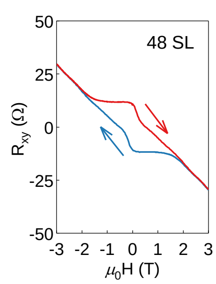

Figure S6. The Hall resistance of the 48 SL sample as a function of out-of-plane magnetic field H at T=2 K, with blue and red arrows indicating the direction of the field scan. The linear ordinary Hall background is removed.

5. Possible physical origin

Here we analyze the possible physical origin of the positive AH+ in detail.

Our first hypothesis is that AH+ originates from an additional surface ferromagnetism. The thickness dependence in Fig. 4 reveals that the positive AH+ vanishes with increasing thickness, indicating that AH+ might be associated with interfacial effects, i.e. an extra surface ferromagnetism. This is possible because the transport becomes dominated by the bulk channels in thicker layers such that AH+ from the surface is no longer distinguishable.

Our second hypothesis is that AH+ originates from hole-mediated RKKY interactions. The gate dependence in Fig. 3 shows that AH+ almost saturates at negative gate voltages and drops rapidly as the gate voltage sweeps from zero to positive. This might indicate that the formation of AH+ strongly relies on the hole carriers, and as the electrons become dominant, AH+ almost vanishes. Therefore, we think AH+ may originate from hole-mediated RKKY (Ruderman–Kittel–Kasuya–Yosida) interactions. RKKY magnetism strongly depends on carriers and is distinct from the carrier-independent van Vleck magnetism. In previous literature, it is agreed that the surface magnetism of an MTI is RKKY-type, while the bulk magnetism of an MTI is van Vleck-type. [1–6] Therefore, our second hypothesis of RKKY origin is also consistent with our first hypothesis of surface ferromagnetism.

Our third hypothesis is that the interfacial $MnTe_2$ monolayer gives rise to the positive AH+. We think that additional phases in our thin films may play an important role in the formation of AH+. From the HAADF-STEM images in Fig. S3, we mainly observed three kinds additional local structures in addition to the dominant $MnBi_2Te_4$ phase: Bi_2Te_3 quintuple layers, $BiTe_2$ monolayers caused by Mn line vacancies in the $MnBi_2Te_4$ septuple layers, and a $MnTe_2$ monolayer that interfaces with Bi_2Te_3 on the surface of the thin film. It is hard for Bi_2Te_3 quintuple layers to give rise to the positive AH+, since they either do not contain magnetic elements and are non-magnetic, or contain Mn dopants and show a negative AHE [3]. Bi_2Te_3 can also work as non-magnetic buffer layers between $MnBi_2Te_4$ and give rise to ferromagnetism in $MnBi_2Te_4/(Bi_2Te_3)_n$ superlattices, but the resulting AHE is still negative. [7–9] To the best of our knowledge, there is also no previous report of $BiTe_2$ monolayers giving rise to a positive AHE. It is most likely that the $MnTe_2$ monolayer gives rise to the positive AH+ since it is ferromagnetic and has perpendicular magnetic anisotropy (PMA) according to first-principles calculations[10,11]. This hypothesis is also consistent with our first hypothesis of surface ferromagnetism.

Our fourth and final hypothesis is that the interfacial $MnTe_2$ monolayer couples with the surface states of topological insulators. It might be possible that the interfacial $MnTe_2$ monolayer alone contributes to the AH+ and all the other layers are not involved. However, this explanation is not consistent with the critical temperature of 25 K for AH+, since the reported Curie temperatures of a $MnTe_2$ monolayer range from 88 K to 440 K[10,11]. Furthermore, AH– and AH+ share the same critical temperature, suggesting that the interfacial $MnTe_2$ monolayer may have a similar mechanism of surface ferromagnetism as the MTI $MnBi_2Te_4$. Therefore, we think that a more likely scenario is that the amount of interfacial $MnTe_2$ might not be enough to support its own ferromagnetism. However, by coupling with the surface states of the topological insulators, the interfacial $MnTe_2$ monolayer might work effectively as additional ferromagnetic dopants on the topological insulator surface to give rise to an extra surface ferromagnetism, which is in addition to the surface ferromagnetism of the MTI $MnBi_2Te_4$ itself [3,12–14]. Both surface ferromagnetisms share the same mechanism, as demonstrated in previous theoretical works, that the Dirac electronic states of a topological insulator mediate an RKKY interaction among the magnetic impurities on its surface, contributing to the surface ferromagnetism. [15–17] Therefore, our fourth and final hypothesis is also consistent with the previous three.

To summarize, we speculate that the additional positive AH+ is due to an extra surface ferromagnetism from the surface-state-mediated RKKY interaction among ferromagnetic impurities on the surface, and the impurities are a $MnTe_2$ monolayer.

References

1. Kou, X. *et al.* Manipulating surface-related ferromagnetism in modulation-doped topological insulators. *Nano Lett.* **13**, 4587–4593 (2013).

2. Kou, X. *et al.* Interplay between different magnetisms in Cr-doped topological insulators. *ACS Nano* **7**, 9205–9212 (2013).

3. Checkelsky, J. G., Ye, J., Onose, Y., Iwasa, Y. & Tokura, Y. Dirac-fermion-mediated ferromagnetism in a topological insulator. *Nat. Phys.* **8**, 729–733 (2012).

4. Chang, C. Z. *et al.* Thin films of magnetically doped topological insulator with carrier-independent long-range ferromagnetic order. *Adv. Mater.* **25**, 1065–1070 (2013).

5. Li, M. *et al.* Experimental verification of the van Vleck nature of long-range ferromagnetic order in the vanadium-doped three-dimensional topological insulator Sb2Te3. *Phys. Rev. Lett.* **114**, 1–5 (2015).

6. Sessi, P. *et al.* Dual nature of magnetic dopants and competing trends in topological insulators. *Nat. Commun.* **7**, 1–6 (2016).

7. Wu, J. *et al.* Natural van der Waals heterostructural single crystals with both magnetic and topological properties. *Sci. Adv.* **5**, 1–10 (2019).

8. Tian, S., Li, H. & Wang, Z. Magnetic topological insulator MnBi6Te10 with a zero-field ferromagnetic state and gapped Dirac surface states. *Phys. Rev. B* **102**, 35144 (2020).

9. Hu, C. *et al.* Realization of an intrinsic ferromagnetic topological state in MnBi8Te13. *Sci. Adv.* **6**, 1–10 (2020).

10. Chen, W., Zhang, J. min, Nie, Y. Z., Xia, Q. L. & Guo, G. H. Electronic structure and magnetism of MTe2 (M = Ti, V, Cr, Mn, Fe, Co and Ni) monolayers. *J. Magn. Magn. Mater.* **508**, (2020).

11. Chen, W., Zhang, J. M., Nie, Y. Z., Xia, Q. L. & Guo, G. H. Tuning magnetic properties of single-layer MnTe2 via strain engineering. *J. Phys. Chem. Solids* **143**, 109489 (2020).

12. Shikin, A. M. *et al.* Nature of the Dirac gap modulation and surface magnetic interaction in axion antiferromagnetic topological insulator MnBi$_2$Te$_4$. *Sci. Rep.* 1–13 (2020). doi:10.1038/s41598-020-70089-9

13. Nevola, D. *et al.* Coexistence of Surface Ferromagnetism and Gapless Topological State in MnBi$_2$Te$_4$. *Phys. Rev. X* **117205**, 1–5 (2020).

14. Liu, W. *et al.* Experimental observation of dual magnetic states in topological insulators. *Sci. Adv.* **5**, 4–10 (2019).

15. Liu, Q., Liu, C. X., Xu, C., Qi, X. L. & Zhang, S. C. Magnetic impurities on the surface of a topological insulator. *Phys. Rev. Lett.* **102**, 1–4 (2009).

16. Biswas, R. R. & Balatsky, A. V. Impurity-induced states on the surface of three-dimensional topological insulators. *Phys. Rev. B* **81**, 1–4 (2010).

17. Rosenberg, G. & Franz, M. Surface magnetic ordering in topological insulators with bulk magnetic dopants. *Phys. Rev. B* **85**, 1–7 (2012).